

PAPER

[View Article Online](#)
[View Journal](#) | [View Issue](#)Cite this: *J. Mater. Chem. A*, 2018, **6**, 21969

Solid-phase hot-pressing synthesis of POMOFs on carbon cloth and derived phosphides for all pH value hydrogen evolution†

Yu-Jia Tang,^{‡a} Yifa Chen,^{‡a} Hong-Jing Zhu,^a A.-Man Zhang,^a Xiao-Li Wang,^a Long-Zhang Dong,^{id}^a Shun-Li Li,^a Qiang Xu^{id}^{*b} and Ya-Qian Lan^{id}^{*a}

Designing an all pH value hydrogen evolution reaction (HER) electrocatalyst with low cost and high activity is urgently needed for future energy storage and conversion systems. Metal–organic frameworks (MOFs) with well-defined pore structures and various metal sources provide feasible platforms for the design of efficient electrocatalysts. However, MOFs as crystalline materials are mostly in crystal or powder form, which would hinder their practical application. Herein, polyoxometalate-based MOFs (POMOFs) were synthesized on carbon cloth (CC) through a facile and general solid-phase hot-pressing method for the first time. The thus-obtained POMOFs/CC can be converted into three phase bimetallic phosphides coated with porous carbon on CC through a phosphidation process, show high electrocatalytic stability over a wide pH range (pH, 0–14) and possess excellent HER performance with low overpotential (e.g., 90.5 mV at 10 mA cm^{−2} in 1 M KOH). Moreover, the POMOFs/CC derived phosphides present high selectivity for H₂ production (nearly 100% faradaic efficiency) and ultra-low charge-transfer resistance (0.96 Ω) in alkaline medium, which hold promise for practical applications. This work provides a powerful strategy for the facile production of fast nucleating MOF-derived electrodes with potential for industrial-scale application in energy storage and conversion.

Received 9th March 2018

Accepted 5th April 2018

DOI: 10.1039/c8ta02219d

rsc.li/materials-a

Introduction

Electrochemical water splitting, comprising the hydrogen evolution reaction (HER) and oxygen evolution reaction (OER), is a promising method to produce renewable energy for eco-friendly energy conversion and storage technologies.^{1–3} Although commercial Pt/C and IrO₂ can serve as efficient HER and OER electrocatalysts with low overpotential and large current density, their high cost and rareness still hinder their further industrial application.^{4,5} Non-noble metal-based catalysts with low cost and high abundance are desperately needed to replace noble benchmark catalysts. To date, a large number of non-noble metal-based catalysts such as sulfides,^{6–8} carbides,^{9–11} phosphides,^{12–15} oxides^{16,17} and their hybrid structures^{18,19} have been investigated. However, most reported non-noble metal-based materials only show significant HER performance in acidic, neutral or alkaline electrolytes.^{20–22} Such pH-restricted HER catalysts might have

drawbacks in practical usage over a wide pH range and their applications in overall water splitting systems are limited. Therefore, the demand for ultra-stable electrocatalysts to satisfy practical applications for HER catalysis at all pH values is urgent while largely unmet.

Recently, transition metal phosphides (TMPs, M_xP_y, M = Mo, W, Fe, Co, etc.) have been studied as inspiring all pH value HER electrocatalysts.^{23–26} Among them, molybdenum phosphide (MoP) and tungsten phosphide (WP) have shown promise as HER electrocatalysts in various electrolytes.^{23,27–29} For example, Sun *et al.* reported that MoP₂ nanosheet arrays on carbon cloth (CC) were used as the HER cathode in acidic, basic and neutral media with low overpotentials at 10 mA cm^{−2}.²³ Moreover, another report demonstrated WP nanorod arrays on CC as the universal-pH 3D HER cathode, which showed small overpotentials at 10 mA cm^{−2} and long-term stability.²⁷ Generally, TMP particles are mixed with additives (*i.e.*, Nafion) to cast onto glassy carbon electrodes for HER catalysis. In the process, there are some drawbacks such as the dispersity of TMP particles or the connection between TMP particles and substrates, which might cause problems in long-term catalysis. Powerful methods that can directly fabricate uniformly dispersed TMP particles on conductive substrates are highly desirable. Besides, it remains a challenge to directly use TMP particles under harsh conditions. Some studies reported that the combination of TMP particles with carbon-based materials could increase the

^aJiangsu Collaborative Innovation Centre of Biomedical Functional Materials, Jiangsu Key Laboratory of New Power Batteries, School of Chemistry and Materials Science, Nanjing Normal University, Nanjing 210023, China. E-mail: yqlan@njnu.edu.cn

^bResearch Institute of Electrochemical Energy, National Institute of Advanced Industrial Science and Technology (AIST), Ikeda, Osaka 563-8577, Japan. E-mail: q.xu@aist.go.jp

† Electronic supplementary information (ESI) available: SEM, TEM, HRTEM, XPS, PXRD, LSV, CV, EIS, tables and so on. See DOI: 10.1039/c8ta02219d

‡ These authors contributed equally to this work.

stability and further enhance their electrocatalytic efficiency.^{30,31} In this work, we intend to explore powerful methods that can *in situ* produce carbon-coated TMP materials on conductive substrates to endow this system with high conductivity, dispersity and stability for efficient HER electrocatalysis.

As a class of porous materials, metal–organic frameworks (MOFs) contain rich metal ions and functional ligands to form regular porous structures and periodic pores.^{32–34} Polyoxometalates (POMs) are composed of anionic metal oxide clusters with diverse structures and abundant high-valence transition metals (Mo, W, V, *etc.*).^{35–37} Polyoxometalate-based MOFs (POMOFs) are a kind of novel crystal material where POMs can be a part of MOF frameworks or reside within the cavities to form intriguing structures.³⁸ As precursors, POMOFs can be pyrolyzed to produce porous carbon-coated nano-sized transition-metal (Mo, W, and V from POMs) oxides or carbides.^{39,40} These derivatives can serve as promising electrocatalysts with advantages such as the following: (1) after carbonization, the obtained composites contain bimetallic components with high specific surface areas and hierarchical pores for efficient mass transfer; and (2) the carbon shell protection derived from MOFs can help to avoid polymerization and degradation of metal nanoparticles in harsh electrolytes. Therefore, POMOFs are ideal precursors with a variety of optional metal sources to precisely control the synthesis of TMP particles with unique structures. However, most reported derivative materials are powders, which need to be deposited onto conductive substrates (*e.g.*, glassy carbon electrode and nickel foam) for further applications. However, the powders on the substrates always have weak interaction and are easy to peel off during the electrocatalytic measurements. Therefore, *in situ* deposition of POMOF precursors on conductive substrates uniformly and firmly is a key factor for preparing TMP particles coated by porous carbon on substrates and directly using them as excellent HER electrodes.

Herein, we introduce a powerful solid-phase hot-pressing method to fabricate POMOFs on carbon cloth (POMOFs/CC) rapidly using an electric iron (Fig. 1).^{41,42} POMOFs are desired

crystal materials that combine the advantages of both POMs and MOFs and can be nucleated rapidly under mild reaction conditions. We hot-press POMOFs on CC using copper acetate ($\text{Cu}(\text{OAc})_2 \cdot \text{H}_2\text{O}$), benzenetricarboxylate (BTC) and POMs as precursors for the following reasons: (1) in the case of copper and BTC, the famous MOFs of HKUST-1, which is made up of the dimeric cupric tetracarboxylate units to form a porous and stable structure, can be synthesized using a simple traditional solvent method;⁴³ and (2) Keggin-type POMs (*e.g.*, PMo_{12} and PW_{12}) have small size (<1 nm), and high stability and water solubility, which could make them the best choice for the structure building of POMOFs.³⁸ Therefore, one guest POM molecule can be encapsulated in each cavity of HKUST-1 to construct POMs@HKUST-1 easily.⁴² Then POMOFs/CC can serve as a self-sacrificing platform to synthesize bimetallic phosphides on CC (Cu-M-P/CC , $\text{M} = \text{Mo}$ or W) through a phosphidation process. During phosphidation, POMs are ideal transition-metal sources for TMP particles. MOFs on the one hand can further provide metal sources to achieve bimetallic catalysis systems, and on the other hand can serve as a precursor for porous carbon shells coated on TMP particles to obtain stable and uniform structures. Produced through such a rapid solid-phase hot-pressing method, Cu-M-P/CC hold promise as efficient HER catalysts with three phase phosphide active species, high electrical conductivity, particle dispersity and pH stability, which present great potential for industrial-scale HER catalysis applications.

Experimental

Chemicals

Sodium dihydrogen phosphate dihydrate ($\text{NaH}_2\text{PO}_4 \cdot 2\text{H}_2\text{O}$, AR), sodium phosphate dibasic anhydrous (Na_2HPO_4 , AR), potassium hydroxide (KOH , $\geq 96\%$), concentrated sulfuric acid (H_2SO_4 , 98%), copper acetate monohydrate ($\text{Cu}(\text{OAc})_2 \cdot \text{H}_2\text{O}$, AR), phosphomolybdic acid ($\text{H}_3\text{PMo}_{12}\text{O}_{40} \cdot n\text{H}_2\text{O}$, PMo_{12}), phosphotungstic acid ($\text{H}_3\text{PW}_{12}\text{O}_{40} \cdot n\text{H}_2\text{O}$, PW_{12}), benzene-1,3,5-tricarboxylic acid (H_3BTC , 98%), red phosphorus (P , AR) and

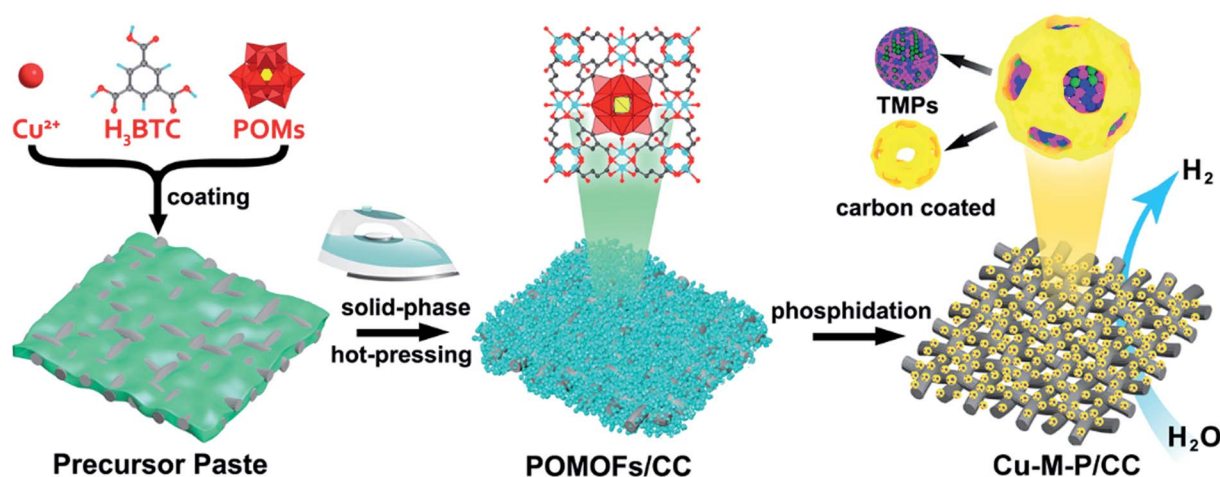


Fig. 1 Schematic representation of the solid-phase hot-pressing synthesis of POMOFs on CC and subsequent preparation of Cu-M-P/CC ($\text{M} = \text{Mo}$ or W).

ethylene glycol ($\text{C}_2\text{H}_6\text{O}_2$, EG, AR) were purchased from Sino-pharm Chemical Reagent Co., Ltd. Polyethylene glycol ($\text{HO}(\text{CH}_2\text{CH}_2\text{O})_n\text{H}$, PEG, MW 4000) was bought from Aladdin Industrial Corporation. 20% Pt/C and Nafion solution (5 wt%) were bought from Sigma-Aldrich. Carbon cloth (CC, W0S1002) was purchased from CeTech Co., Ltd.

Preparation of POMs@HKUST-1/CC

A mixture of $\text{Cu}(\text{OAc})_2 \cdot \text{H}_2\text{O}$ (0.20 g, 1 mmol), PMo_{12} (0.17 g, 0.093 mmol), H_3BTC (0.14 g, 0.67 mmol), 0.10 g PEG and 0.4 mL EG was added into a mortar and ground to form a homogeneous green paste. Then the paste was coated onto both sides of CC (size, $1 \times 2 \text{ cm}^2$) with a thickness of about 0.5 mm. The CC was wrapped with aluminum foil and hot-pressed using an electric iron at 200°C for 20 min. After peeling off the aluminum foil, PMo_{12} @HKUST-1/CC can be obtained. PMo_{12} @HKUST-1/CC with different PMo_{12} loadings was also prepared using smaller PMo_{12} amounts (0.1 g, 0.055 mmol) and excess PMo_{12} amounts (0.3 g, 0.16 mmol), respectively. For comparison, PW_{12} @HKUST-1/CC was synthesized similar to PMo_{12} @HKUST-1/CC except that PW_{12} was used instead of PMo_{12} . Different PW_{12} loadings were studied including 0.14 g (0.055 mmol), 0.26 g (0.093 mmol) and 0.46 g (0.16 mmol). Besides, HKUST-1/CC was prepared without PMo_{12} loadings. PMo_{12} /CC was prepared using PMo_{12} (0.17 g, 0.093 mmol) and 0.1 g PEG as the precursors. PW_{12} /CC was prepared using PW_{12} (0.26 g, 0.093 mmol) and 0.1 g PEG as the precursors.

Preparation of Cu-M-P/CC

Two slices of PMo_{12} @HKUST-1/CC in a quartz crucible were placed in a horizontal tube furnace with 0.2 g of red phosphorus at the upstream side. The samples were heated to 400°C for 2 h and then 800°C for 2 h at a heating speed of 5°C min^{-1} under a N_2 atmosphere. After cooling down to room temperature, Cu-Mo-P/CC was obtained. For comparison, the Cu-W-P/CC composite was prepared by phosphidation of PW_{12} @HKUST-1/CC directly. $\text{Cu}_3\text{P/CuP}_2\text{/CC}$, MoP/CC and WP/CC were prepared by phosphidation of HKUST-1/CC, PMo_{12} /CC and PW_{12} /CC, respectively.

Material characterization

Powder X-ray diffraction (PXRD) patterns were recorded on a D/max 2500VL/PC diffractometer (Japan) equipped with a graphite monochromatized $\text{Cu K}\alpha$ radiation source ($\lambda = 1.54060 \text{ \AA}$). The corresponding working voltage and current are 40 kV and 100 mA, respectively. Transmission electron microscopy (TEM) and high-resolution TEM (HRTEM) images were recorded on JEOL-2100F apparatus at an accelerating voltage of 200 kV. Morphological and microstructural analysis was conducted using a scanning electron microscope (SEM, JSM-7600F) at an accelerating voltage of 10 kV. Energy dispersive X-ray spectroscopy (EDS) was performed with a JSM-5160LV-Vantage type energy spectrometer. Nitrogen adsorption-desorption isotherms were recorded at 77 K using a Quantachrome instrument. X-ray photoelectron spectroscopy (XPS) was performed on a scanning X-ray microprobe (PHI 5000 Versa, ULAC-PHI, Inc.) using

Al $\text{K}\alpha$ radiation and the C 1s peak at 284.8 eV as the internal standard. Inductively coupled plasma optical emission spectrometry (ICP-OES, Leeman Labs) was used to measure the content of metal ions. Hydrogen amounts were analyzed using a gas chromatograph (GC-7900, CEAULight, China) equipped with a thermal conductivity detector (TCD).

Electrochemical measurements

HER measurements in different electrolytes including acidic (0.5 M H_2SO_4), alkaline (1 M KOH) and neutral (0.5 M PBS) media were performed on an electrochemical workstation (Biologic, SP-150) with a three-electrode system. A saturated calomel electrode (SCE) and graphite rod were used as the reference and counter electrodes, respectively. Cu-Mo-P/CC ($1 \times 2 \text{ cm}^2$) was directly used as the working electrode with an average mass loading of 1.37 mg cm^{-2} . The testing area is 1 cm^2 . For the commercial 20% Pt/C catalyst test, 10 mg of sample was added into 0.75 mL of H_2O , 0.20 mL of ethanol and 50 μL of 5 wt% Nafion and sonicated to form a homogeneous mixture (10 mg mL^{-1}). Then 137 μL of the mixture was dropped onto CC substrates with a coating area of $1 \times 1 \text{ cm}^2$. All polarization curves were iR -corrected. The stability tests were conducted by continuous CV cycling from 0 V to -0.3 V vs. RHE at a scan rate of 100 mV s^{-1} . Electrochemical impedance spectroscopy (EIS) was carried out in the frequency range of 1000 kHz to 10 mHz with an AC amplitude of 10 mV at an overpotential of 150 mV vs. RHE. The working potential vs. SCE was converted to the reversible hydrogen electrode (RHE) scale according to the equation $E_{\text{RHE}} = E_{\text{SCE}} + 0.059\text{pH} + 0.245$. Determination of the amounts of H_2 and the faradaic efficiency (FE) was conducted in a gas-tight H-type electrolytic cell and by gas chromatography (GC). Every electrode chamber has a total volume of 150 mL and injects 75 mL electrolyte. A CA test was carried out for 160 min in 1 M KOH at a fixed potential to reach a current density of 10 mA cm^{-2} . 100 μL of gas was extracted at equal intervals of 20 min and injected into the GC. FE was calculated according to the following equation: $\text{FE} = 2nF/Q$, where n (mol) is the total amount of the as-produced H_2 , F (96485 C mol^{-1}) is the Faraday constant, Q (C) is the total voltammetric charge, and 2 indicates the two-electron process per mole of H_2 for the HER.

Results and discussion

Compared with traditional liquid phase synthesis, the solid-phase hot-pressing method for the preparation of POMOFs has the advantages of fast reaction rate and high yield, as well as being solvent-free. The fabrication process of POMOFs/CC and subsequently Cu-M-P/CC is described as follows (Fig. 1). Firstly, a paste containing a mixture of $\text{Cu}(\text{OAc})_2 \cdot \text{H}_2\text{O}$, BTC, POMs, polyethylene glycol (PEG) and a few drops of ethylene glycol (EG) was ground and uniformly painted onto a CC (size, $1 \times 2 \text{ cm}^2$) with a paste thickness of 0.5 mm on both sides. A piece of aluminum foil was covered on the surface of the CC and then hot-pressing was conducted on both sides (*ca.* 200°C , 20 min) to achieve POMOFs/CC. POMs can be encapsulated within the cavities of HKUST-1 to form POMOFs with the formula

$[\text{Cu}_2(\text{BTC})_{4/3}(\text{H}_2\text{O})_2]_6[\text{POMs}] \cdot x\text{H}_2\text{O}$, which are denoted as POMs@HKUST-1. Secondly, a phosphidation procedure using red phosphorus as the P source was applied to transfer POMOFs/CC into Cu-M-P/CC (*i.e.*, Cu-Mo-P/CC and Cu-W-P/CC). The average mass loading of Cu-Mo-P on CC is 1.37 mg cm^{-2} (Table S1†). Notably, PEG was used as the adhesive to ensure that the POMOF precursors grew on the CC substrates tightly and served as the carbon source for phosphidation. In contrast, $\text{Cu}_3\text{P}/\text{CuP}_2/\text{CC}$ and MoP/CC were synthesized by phosphidation of HKUST-1/CC and $\text{PMo}_{12}/\text{CC}$, respectively.

Two POMs@HKUST-1/CC (*i.e.*, $\text{PMo}_{12}/\text{HKUST-1/CC}$ and $\text{PW}_{12}/\text{HKUST-1/CC}$) were investigated in this work. The powder X-ray diffraction (PXRD) patterns show that the peaks of $\text{PMo}_{12}/\text{HKUST-1/CC}$ and $\text{PW}_{12}/\text{HKUST-1/CC}$ match well with the simulated pattern of POMOFs (Fig. 2a). As a comparison, HKUST-1/CC was fabricated following the same hot-pressing procedures without POMs and the PXRD pattern of HKUST-1/CC is consistent with the simulated one (Fig. 2a). A clear illustration of the crystal structures of POMs, HKUST-1 and POMs@HKUST-1 is provided in Fig. S1†. Single crystals of POMs@HKUST-1 were formed by the co-crystallization of POMs and HKUST-1 rather than from a simple mixture. Additionally, the most obvious difference of PXRD patterns between POMs@HKUST-1 and HKUST-1 is that the first strong peak is at different 2 theta degrees. After introducing POMs into the cavities of HKUST-1, the first strong peak at 6.7° has a left shift to 5.8° to form POMOFs. The CCDC reference number of $\text{PMo}_{12}/\text{HKUST-1}$, $\text{PW}_{12}/\text{HKUST-1}$ and HKUST-1 is 686797, 686795 and 112954, respectively, which can be found in the Cambridge Structural Database with detailed crystallographic data in CIF.^{42,43} After phosphidation, taking Cu-Mo-P/CC for example, the PXRD pattern of Cu-Mo-P/CC derived from $\text{PMo}_{12}/\text{HKUST-1/CC}$ exhibits a mixed-phase pattern (Fig. 2b). Three phases including molybdenum phosphide of MoP (JCPDS no. 24-771) and copper phosphides of Cu_3P (JCPDS no. 71-2261) and CuP_2 (JCPDS no. 65-6208) are detected. Similar results are

also obtained from the PXRD pattern of Cu-W-P/CC derived from $\text{PW}_{12}/\text{HKUST-1/CC}$. Three phases including Cu_3P , CuP_2 and tungsten phosphide of WP (JCPDS no. 29-1364) are identified. As a comparison, $\text{Cu}_3\text{P}/\text{CuP}_2/\text{CC}$ derived from HKUST-1/CC shows two phases of Cu_3P and CuP_2 .

Prepared from the solid-phase hot-pressing method, the obtained device exhibits high particle dispersity. For instance, $\text{PMo}_{12}/\text{HKUST-1}$ nanoparticles are uniformly dispersed on CC, verified by the scanning electron microscopy (SEM) and transmission electron microscopy (TEM) images (Fig. S2†). After phosphidation, flexible Cu-Mo-P/CC having a black color was produced (size, $2 \times 2 \text{ cm}^2$) (Fig. 3a). The SEM images of Cu-Mo-P/CC at different magnifications demonstrate that Cu-Mo-P nanoparticles (average size, *ca.* 100 nm) are uniformly decorated on every single string of carbon fiber in Cu-Mo-P/CC (Fig. 3b). The uniformly dispersed morphology of Cu-Mo-P nanoparticles was also confirmed by the TEM image (Fig. 3c). To further investigate the structure and composition of Cu-Mo-P nanoparticles, a high-resolution TEM (HRTEM) test is performed (Fig. 3d). In particular, three kinds of TMP phases (*i.e.*, MoP, Cu_3P and CuP_2) are detected and embedded in amorphous porous carbon in the Cu-Mo-P nanoparticles, indicating the strong electronic interactions among these phosphide particles. This result is also verified by the high-angle annular dark-field (HADF) image and energy dispersive spectroscopy (EDS) element mapping (Fig. 3e). Therefore, derived from $\text{PMo}_{12}/\text{HKUST-1/CC}$, Cu-Mo-P nanoparticles are uniformly dispersed on CC and present an amorphous carbon coated morphology. The porosity of Cu-Mo-P/CC, $\text{Cu}_3\text{P}/\text{CuP}_2/\text{CC}$ and MoP/CC is also investigated. Notably, Cu-Mo-P/CC has a Brunauer-Emmett-Teller (BET) specific surface area of $40.2 \text{ m}^2 \text{ g}^{-1}$, supported by the N_2 adsorption-desorption test (Fig. S3a†), which is much higher than those of the contrast samples of $\text{Cu}_3\text{P}/\text{CuP}_2/\text{CC}$ ($39.8 \text{ m}^2 \text{ g}^{-1}$) and MoP/CC ($36.4 \text{ m}^2 \text{ g}^{-1}$).⁴⁴ Besides, the total pore volumes of Cu-Mo-P/CC, $\text{Cu}_3\text{P}/\text{CuP}_2/\text{CC}$ and MoP/CC are $5.4 \times 10^{-2} \text{ cm}^3 \text{ g}^{-1}$, $3.6 \times 10^{-2} \text{ cm}^3 \text{ g}^{-1}$ and

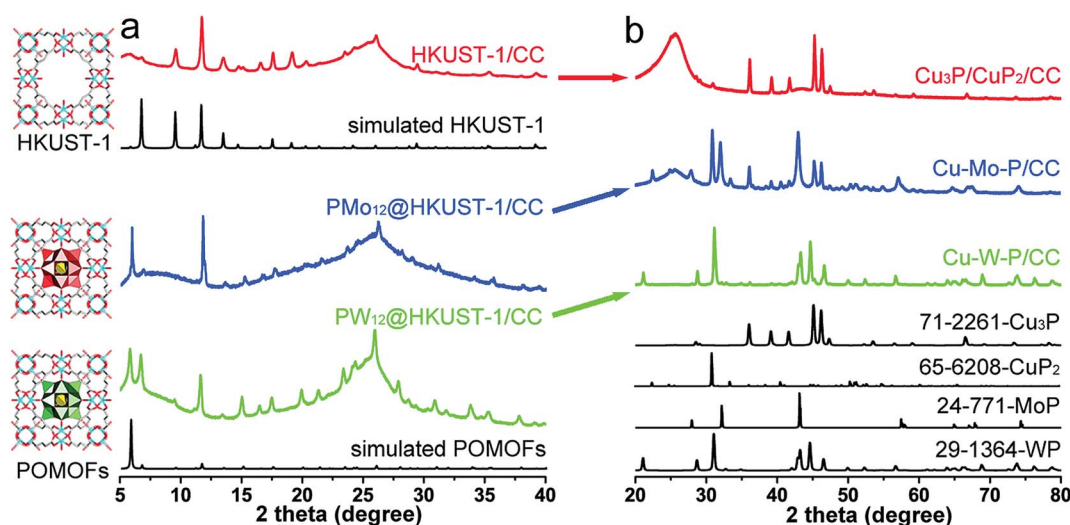


Fig. 2 (a) Crystal structures and PXRD patterns of HKUST-1 and POMOFs on CC. (b) PXRD patterns of $\text{Cu}_3\text{P}/\text{CuP}_2/\text{CC}$, Cu-Mo-P/CC and Cu-W-P/CC synthesized through phosphidation and the corresponding simulated patterns.

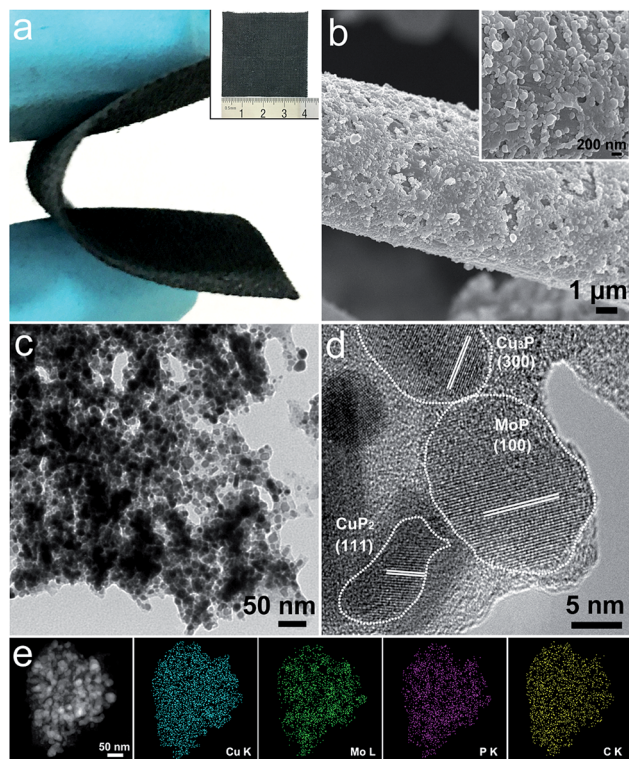


Fig. 3 (a) Photo image of Cu-Mo-P/CC ($2 \times 2 \text{ cm}^2$). (b) SEM images of Cu-Mo-P/CC obtained at different magnifications. (c) TEM image of Cu-Mo-P sonicated from the CC substrate. (d) HRTEM image of Cu-Mo-P. The lattice spacings of 0.278, 0.200 and 0.289 nm are assigned to the (100), (300) and (111) planes of MoP, Cu_3P and CuP_2 , respectively. (e) HADDF image and the corresponding element mapping of Cu-Mo-P. Cu, Mo, P and C are shown in blue, green, purple and yellow, respectively.

$3.9 \times 10^{-2} \text{ cm}^3 \text{ g}^{-1}$, respectively. The above three samples all show hierarchical porosity with pore size distributions ranging from 2.5 nm to 35 nm (Fig. S3b†). As control experiments, the morphologies of HKUST-1/CC and PMo_{12} /CC and their derivatives using SEM, TEM and HRTEM images are also tested and shown in Fig. S4 to S6.† Moreover, large area SEM images of Cu-Mo-P/CC, $\text{Cu}_3\text{P}/\text{CuP}_2/\text{CC}$ and MoP/CC are shown in Fig. S7,† further proving the advantages of Cu-Mo-P particles on CC without stacking.

With high particle dispersity, amorphous carbon coated morphology and hierarchical porosity, Cu-Mo-P/CC also possesses a large amount of active species. The surface chemical states of Cu-Mo-P/CC were studied by X-ray photoelectron spectroscopy (XPS) to illustrate the potential active species in the film. The spectra of Cu, Mo, P, C and O are displayed in Fig. S8a.† Based on the XPS data, the molar ratio of Cu/Mo for Cu-Mo-P/CC is about 0.78 : 1, which is consistent with the molar ratio in precursors and the formula of POMOFs (Table S2†). Inductively coupled plasma optical emission spectrometry (ICP-OES) is also used to analyze the Cu/Mo molar ratio of Cu-Mo-P particles (0.96 : 1), which is very close to the Cu/Mo molar ratio in the raw materials. The Cu 2p spectrum (Fig. S8b†) shows two main peaks of Cu $2p_{1/2}$ and Cu $2p_{3/2}$ along with their

corresponding satellite peaks.⁴⁵ The Cu $2p_{1/2}$ region exhibits two deconvoluted peaks at 954.9 and 952.4 eV, attributed to Cu^{2+} and Cu^{1+} , respectively. Similarly, the Cu $2p_{3/2}$ region gives Cu^{2+} at 934.8 eV and Cu^{1+} at 932.5 eV. The majority (63.2%) of Cu^{1+} in Cu 2p belongs to the metal-rich Cu_3P , which can improve the conductivity and facilitate the electron transfer of Cu-Mo-P/CC. Besides, the Mo 3d spectrum can be deconvoluted into six peaks with different valence states (Fig. S8c†). The two main peaks at 231.3 eV and 228.1 eV can be ascribed to MoP.⁴⁶ The other four peaks are assigned to the partially oxidized form of MoO_x on the Cu-Mo-P/CC surface. Notably, the electron binding energies of Cu $2p_{1/2}$ and Cu $2p_{3/2}$ of Cu-Mo-P/CC both have a negative shift of ~ 0.7 eV compared with the Cu 2p spectrum of $\text{Cu}_3\text{P}/\text{CuP}_2/\text{CC}$. Both $\text{Mo}^{\delta+} 3d_{3/2}$ and $\text{Mo}^{\delta+} 3d_{5/2}$ also exhibit a negative shift of ~ 0.2 eV in contrast to the Mo 3d spectrum of MoP/CC. These results prove the strong electronic interactions among the MoP, Cu_3P and CuP_2 species, implying the successful hybridization of Cu-Mo-P nanoparticles on CC. Furthermore, the P 2p spectrum shows the binding energies of P $2p_{1/2}$ and P $2p_{3/2}$ at 130.3 and 129.5 eV, respectively, suggesting the successful preparation of phosphides (Fig. S8d†). The C 1s spectrum mainly contains C-C/C=C and C-O bonds (Fig. S8e†). Also the O 1s spectrum in Fig. S8f† can be deconvoluted into O-C/O=C and O-OH bonds. As a comparison, the XPS spectra of $\text{Cu}_3\text{P}/\text{CuP}_2/\text{CC}$ and MoP/CC are also presented in Fig. S9 and S10 in detail.† The surface chemical state results imply that Cu-Mo-P/CC is a kind of efficient catalyst with a large amount of active sites.

Above all, Cu-Mo-P/CC with the advantages of an amorphous carbon coated morphology, high dispersity, hierarchical porosity and a large amount of three phase phosphide active species might serve as an efficient electrocatalyst for the HER. To estimate the electrocatalytic activity for the HER, Cu-Mo-P/CC and other contrast samples (*i.e.*, 20% Pt/C, $\text{Cu}_3\text{P}/\text{CuP}_2/\text{CC}$ and MoP/CC) were directly used as the working electrodes. Three kinds of electrolytes including 0.5 M H_2SO_4 (pH = 0), 1 M KOH (pH = 14) and 0.5 M PBS (pH = 6.8), which cover all pH ranges, were applied for measurements. All the polarization curves are shown with iR compensation. As a control experiment, the HER performance of bare CC was also investigated in all-pH value electrolytes to eliminate the effects of substrates (Fig. S11†).

Various phosphidation temperatures (*i.e.*, 700, 800 and 900 °C) were studied for Cu-Mo-P/CC. Based on the linear scan voltammogram (LSV) curves, the lowest overpotentials (η_{10} , acidic 145.9 mV; alkaline 90.5 mV) are achieved at 800 °C, which implies that it is the best phosphidation temperature (Fig. S12†). Moreover, the performances of Cu-Mo-P/CC in different electrolytes were also investigated. The LSV curves in Fig. 4a show that Cu-Mo-P/CC has an overpotential of 145.9 mV vs. RHE at a current density of 10 mA cm^{-2} , which is much lower than those of $\text{Cu}_3\text{P}/\text{CuP}_2/\text{CC}$ (266.1 mV) and MoP/CC (223.6 mV) and close to that of 20% Pt/C (58 mV) in acidic medium. In alkaline medium (1 M KOH), the onset potential and η_{10} of Cu-Mo-P/CC are ~ 15 mV and 90.5 mV, respectively. Remarkably, this result is close to that of commercial Pt/C catalyst (onset potential, 0 mV and η_{10} , 29 mV) (Fig. 4b and 5a). In contrast, both $\text{Cu}_3\text{P}/\text{CuP}_2/\text{CC}$ and MoP/CC give higher onset potential

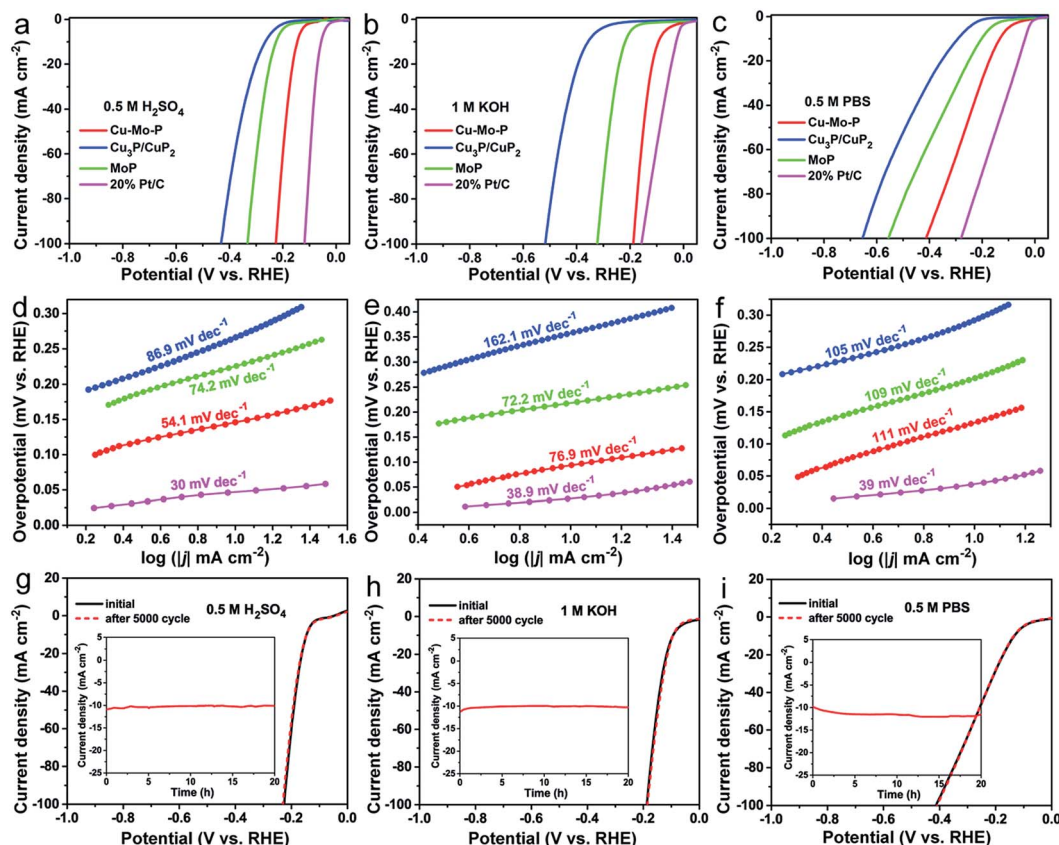


Fig. 4 (a–c) LSV curves and (d–f) Tafel slopes of Cu–Mo–P/CC, Cu₃P/CuP₂/CC, MoP/CC and commercial 20% Pt/C in 0.5 M H₂SO₄, 1 M KOH and 0.5 M PBS, respectively. (g–i) LSV curves of Cu–Mo–P/CC before and after 5000 CV cycles in 0.5 M H₂SO₄, 1 M KOH and 0.5 M PBS, respectively. The insets are the corresponding chronoamperometric curves.

(225.1 and 132.6 mV) as well as η_{10} (358.7 and 220.2 mV) than Cu–Mo–P/CC in 1 M KOH, respectively (Fig. 4b). In 0.5 M PBS, Cu–Mo–P/CC also presents superior HER performance with η_{10}

of 132.6 mV compared to Cu₃P/CuP₂/CC (294.8 mV) and MoP/CC (202.2 mV) (Fig. 4c).

The Tafel slope is an important parameter that reflects the rate-controlling step for the HER (Fig. 4d–f). The Tafel slopes of Cu–Mo–P/CC are 54.1, 76.9 and 111 mV dec⁻¹ in acidic, alkaline and neutral medium, respectively. The Tafel slopes of Cu–Mo–P/CC in different electrolytes are in the range from 40 to 120 mV dec⁻¹, revealing the Volmer–Heyrovsky mechanism during the HER process.^{47,48} In comparison, Cu₃P/CuP₂/CC and MoP/CC both give higher Tafel slopes than Cu–Mo–P/CC at all pH values, demonstrating the relatively sluggish electron transfer and slow electrocatalytic reaction rates (e.g., Cu₃P/CuP₂/CC, 162.1 mV dec⁻¹ in alkaline medium and MoP/CC, 109 mV dec⁻¹ in neutral medium) (Table S3†). Noteworthy, the Tafel slope of Cu–Mo–P/CC in acidic medium is the lowest among all contrast samples and is close to that of the commercial Pt/C catalyst (30 mV dec⁻¹).¹ In general, the performance of Cu–Mo–P/CC in the entire pH range is among the best for MOF-derived materials and other phosphides on substrates, such as CoP/CC,²⁴ CoSe₂/CF⁴⁹ and Cu₃P NW/CF⁵⁰ (Table S4†). To highlight the advantages of the solid-phase hot-pressing method, a traditional liquid-phase stirring method was used to prepare PMo₁₂@HKUST-1, which was further treated with a similar phosphidation process to obtain Cu–Mo–P powder.⁴⁰ Then the Cu–Mo–P powder was mixed with Nafion and further attached

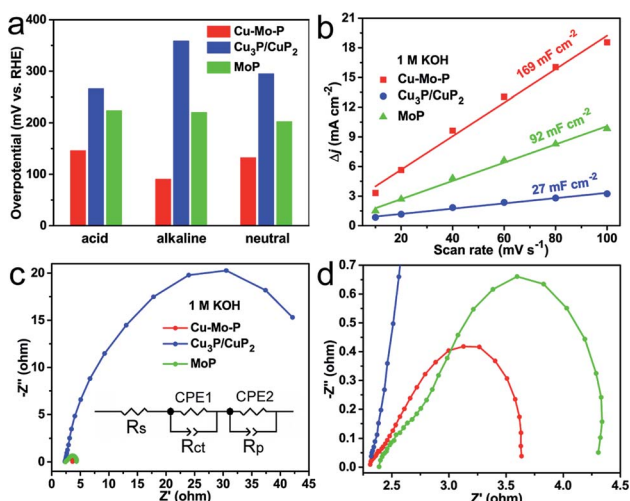


Fig. 5 (a) The comparison of η_{10} of Cu–Mo–P/CC, Cu₃P/CuP₂/CC and MoP/CC in different electrolytes. (b) Double-layer capacitance of Cu–Mo–P/CC, Cu₃P/CuP₂/CC, and MoP/CC calculated according to the CV curves in 1 M KOH. (c) EIS spectrum recorded at an overpotential of 150 mV vs. RHE in 1 M KOH; the inset is the equivalent circuit model. (d) The enlarged spectrum in the high frequency region in (c).

onto the surface of CC to investigate the HER performance. In particular, it shows poorer HER performance than Cu–Mo–P/CC (Fig. S13†). This might be attributed to the better particle dispersity and tighter connections between Cu–Mo–P nanoparticles and CC in Cu–Mo–P/CC than in the electrode fabricated through the secondary fabrication process.

Furthermore, fabricated through the hot-pressing method, Cu–Mo–P nanoparticles with diverse compositions can be achieved on CC. Adjusting the amount of PMo_{12} (*i.e.*, 0.055 mmol, 0.093 mmol and 0.16 mmol) added to the precursor, different Cu–Mo–P/CC samples with various Mo loadings were achieved. The LSV curves and Tafel slopes of Cu–Mo–P/CC were measured to compare their HER performance in different electrolytes (Fig. S14†). Cu–Mo–P/CC with the medium mass loading of 0.093 mmol PMo_{12} in the precursor (Cu/Mo molar ratio is *ca.* 1 : 1) shows better HER performance than the less loaded or excess loaded samples in the all pH value electrolytes. Apart from Cu–Mo–P/CC, other catalysis systems were also investigated. For example, Cu–W–P/CC can be produced from the phosphidation of $\text{PW}_{12}@HKUST-1/\text{CC}$. The structure is similar to that of $\text{PMo}_{12}@HKUST-1$ except that the POM in the central cavity is PW_{12} . This provides a good platform to compare the HER performance of similar phosphides with different chemical compositions. The LSV curves and Tafel slopes of Cu–W–P/CC with different PW_{12} loadings were also investigated in different electrolytes (Fig. S15†). Cu–W–P/CC presents better HER performance with higher PW_{12} loadings in the precursors. For instance, Cu–W–P/CC with the highest PW_{12} loading (0.16 mmol in the precursor) possesses the best activity in 1 M KOH (η_{10} , 167.6 mV and Tafel slope, 110.5 mV dec^{-1}). However, the HER performance of Cu–W–P/CC is still not as good as that of Cu–Mo–P/CC. This might be attributed to the higher HER activity of Mo than W, which can be proved by the HER activity comparison between MoP/CC and WP/CC. As shown in Fig. S16,† the WP/CC electrode has more negative onset overpotentials and higher η_{10} than MoP/CC in all pH value electrolytes. This work will focus on the Cu–Mo–P/CC sample with the best Mo loading to further investigate the HER performance.

The long-term stability is one of the critical prerequisites for practical applications, since it determines the durability of the electrocatalysts under harsh conditions. Remarkably, Cu–Mo–P/CC presents excellent long-term stability. The LSV curves of Cu–Mo–P/CC recorded before and after 5000 cyclic voltammetry (CV) cycles (ranging from 0 to -0.3 V *vs.* RHE.) almost overlap for the three kinds of electrolytes (Fig. 4g–i). Moreover, Cu–Mo–P/CC exhibits almost no degradation after continuous chronoamperometric (CA) electrolysis for 20 h, showing 93% retention in 0.5 M H_2SO_4 and 92% retention in 1 M KOH and even a little increase of current density in 0.5 M PBS (inset images in Fig. 4g–i).

To further realize the excellent HER electroactivity of Cu–Mo–P/CC, the electrochemically active surface area (ECSA) was examined and electrochemical impedance spectroscopy (EIS) performed. The double-layer capacitance (C_{dl}) at the solid-liquid interface is proportional to the ECSA, which can be calculated to analyze the assessable HER electroactivity. In 1 M KOH, the C_{dl} value of Cu–Mo–P/CC calculated from the CV plot

is 169 mF cm^{-2} , which is 6.3-fold and 1.8-fold higher than those of $\text{Cu}_3\text{P}/\text{CuP}_2/\text{CC}$ (27 mF cm^{-2}) and MoP/CC (92 mF cm^{-2}) (Fig. 5b and S17†). This result fits well with the HER activities and similar trends of the C_{dl} values are observed under acidic and PBS conditions (Fig. S18 and S19†). As shown in the EIS spectra, all samples reveal semicircles in the three kinds of electrolytes and show low charge-transfer resistance (R_{ct}) in the high frequency range (Fig. 5c and d and S20 and Table S5†). For instance, the R_{ct} values of Cu–Mo–P/CC, $\text{Cu}_3\text{P}/\text{CuP}_2/\text{CC}$, and MoP/CC recorded at an overpotential of 150 mV *vs.* RHE in 1 M KOH are 0.96, 48.8 and 1.3 Ω , respectively, which are fitted according to the equivalent circuit in the inset of Fig. 5c. The ultra-low R_{ct} value of Cu–Mo–P/CC indicates fast charge-transfer kinetic and high ionic conductivity, which is beneficial for the HER performance.

The excellent performance and high long-term stability provide a fundamental basis for further applications. We set out to investigate the hydrogen production amount of Cu–Mo–P/CC. A hydrogen production test was conducted in the cathode compartment of a gas-tight H-type electrolytic cell. In the test, CA was carried out in 1 M KOH for 160 min at a fixed overpotential to reach a current density of 10 mA cm^{-2} and faradaic efficiency (FE) was calculated by comparing the measured and theoretical H_2 amounts. As shown in Fig. S21,† Cu–Mo–P/CC has nearly 100% FE, and its H_2 production is close to the theoretical value, suggesting a high selectivity for the HER.

A series of physical characterization experiments of Cu–Mo–P/CC after the HER test were carried out to prove the high stability. The morphology of Cu–Mo–P/CC after the CA test for 20 h at all pH values is almost unaffected compared with the as-synthesized one, proved by SEM images (Fig. 3b and S22†). A leaching test was also conducted by ICP-OES to reflect the catalytic stability of Cu–Mo–P/CC. Taking acid electrolyte (*i.e.*, 0.5 M H_2SO_4) for example, only $9.38 \times 10^{-10} \text{ mol mL}^{-1}$ and $9.30 \times 10^{-10} \text{ mol mL}^{-1}$ concentrations of dissolved Mo and Cu were detected after 20 h of CA testing. The dissolved mass percents of Mo and Cu were 1.3 wt% and 1.9 wt% with an electrolyte volume of 30 mL and a measured mass of 1.37 mg for Cu–Mo–P catalysts. These data indicate the high stability of Cu–Mo–P/CC during the stability tests. In spite of the retained catalytic performance and high stability after 20 h of CA testing, a special phase-transformation (CuP_2 was transformed into Cu_3P) was observed by PXRD and XPS tests and the real active species are Cu_3P and MoP for Cu–Mo–P/CC in the HER catalysis (Fig. S23 and S24†). The high stability of Cu–Mo–P/CC might be attributed to the porous carbon coated morphology of Cu–Mo–P nanoparticles and tight adhesion of Cu–Mo–P nanoparticles on CC, which prevent Cu–Mo–P particles from corrosion in harsh electrolytes and ensure the long-term stability. To further clarify the hypothesis, photographs of the electrolyte before and after 5000 CV cycles were taken. After 5000 CV cycles, no color change was observed (Fig. S25†).

Conclusions

In summary, we report a powerful solid-phase hot-pressing method to fabricate POMOFs ($\text{PMo}_{12}@HKUST-1/\text{CC}$ and

PW₁₂@HKUST-1/CC) on CC rapidly for the first time. This facile and non-polluting method perfectly solves the problem that MOF materials are easy to peel off from the substrates. The unique structure of POMOFs with POM particles encapsulated in the cavities of HKUST-1 ensures the subsequent phosphidation to synthesize Cu-M-P/CC (M = Mo or W), which possess a porous carbon coated morphology, uniform dispersion and strong electronic interactions of nanoparticles on CC, hierarchical porosity and a large amount of three phase active phosphide species. All these advantages make Cu-M-P/CC a promising HER electrocatalyst. Taking Cu-Mo-P/CC for example, it shows high catalysis stability and excellent HER performance with low overpotential over a wide pH range (e.g., 90.5 mV at 10 mA cm⁻² in 1 M KOH), demonstrating one of the best HER performances among recently reported MOF-derived materials and other phosphides on substrates. Notably, Cu-Mo-P/CC presents high selectivity for H₂ production (nearly 100% FE) and ultra-low charge-transfer resistance (0.96 Ω). It is indicated that the preparation of fast nucleating MOFs onto conductive substrates in quantity through such a facile solid-phase hot-pressing method holds promising applications for electrochemical reactions and future energy devices.

Conflicts of interest

There are no conflicts to declare.

Acknowledgements

This work was financially supported by the National Natural Science Foundation of China (No. 21622104, 21371099 and 21471080), the NSF of Jiangsu Province of China (No. BK20141445), the Postgraduate Research & Practice Innovation Program of Jiangsu Province (No. KYCX17_1060), the Priority Academic Program Development of Jiangsu Higher Education Institutions, the Foundation of Jiangsu Collaborative Innovation Center of Biomedical Functional Materials and the China Postdoctoral Science Foundation (No. 2016M590475).

Notes and references

- 1 C. C. L. McCrory, S. Jung, I. M. Ferrer, S. M. Chatman, J. C. Peters and T. F. Jaramillo, *J. Am. Chem. Soc.*, 2015, **137**, 4347–4357.
- 2 M. Fang, G. Dong, R. Wei and J. C. Ho, *Adv. Energy Mater.*, 2017, **7**, 1700559.
- 3 M. G. Walter, E. L. Warren, J. R. McKone, S. W. Boettcher, Q. Mi, E. A. Santori and N. S. Lewis, *Chem. Rev.*, 2010, **110**, 6446–6473.
- 4 Z. Pu, I. S. Amiinu, Z. Kou, W. Li and S. Mu, *Angew. Chem., Int. Ed.*, 2017, **56**, 11559–11564.
- 5 Y. Lee, J. Suntivich, K. J. May, E. E. Perry and Y. Shao-Horn, *J. Phys. Chem. Lett.*, 2012, **3**, 399–404.
- 6 P. Chen, T. Zhou, M. Chen, Y. Tong, N. Zhang, X. Peng, W. Chu, X. Wu, C. Wu and Y. Xie, *ACS Catal.*, 2017, **7**, 7405–7411.
- 7 R. Miao, B. Dutta, S. Sahoo, J. He, W. Zhong, S. A. Cetegen, T. Jiang, S. P. Alpay and S. L. Suib, *J. Am. Chem. Soc.*, 2017, **139**, 13604–13607.
- 8 T. Tian, L. Huang, L. Ai and J. Jiang, *J. Mater. Chem. A*, 2017, **5**, 20985–20992.
- 9 K. Xu, H. Ding, H. Lv, P. Chen, X. Lu, H. Cheng, T. Zhou, S. Liu, X. Wu, C. Wu and Y. Xie, *Adv. Mater.*, 2016, **28**, 3326–3332.
- 10 Z. Cui, Y. Li, G. Fu, X. Li and J. B. Goodenough, *Adv. Mater.*, 2017, **29**, 1702385–1702391.
- 11 J. Jiang, Q. Liu, C. Zeng and L. Ai, *J. Mater. Chem. A*, 2017, **5**, 16929–16935.
- 12 Y. Xu, R. Wu, J. Zhang, Y. Shi and B. Zhang, *Chem. Commun.*, 2013, **49**, 6656–6658.
- 13 T. Liu, D. Liu, F. Qu, D. Wang, L. Zhang, R. Ge, S. Hao, Y. Ma, G. Du, A. M. Asiri, L. Chen and X. Sun, *Adv. Energy Mater.*, 2017, **7**, 1700020.
- 14 L. Ai, Z. Niu and J. Jiang, *Electrochim. Acta*, 2017, **242**, 355–363.
- 15 L. Ai, T. Tian and J. Jiang, *ACS Sustainable Chem. Eng.*, 2017, **5**, 4771–4777.
- 16 M. Tahir, L. Pan, R. Zhang, Y.-C. Wang, G. Shen, I. Aslam, M. A. Qadeer, N. Mahmood, W. Xu, L. Wang, X. Zhang and J.-J. Zou, *ACS Energy Lett.*, 2017, **2**, 2177–2182.
- 17 Y. P. Zhu, T. Y. Ma, M. Jaroniec and S. Z. Qiao, *Angew. Chem., Int. Ed.*, 2017, **56**, 1324–1328.
- 18 Y. Zhang, X. Xia, X. Cao, B. Zhang, N. H. Tiep, H. He, S. Chen, Y. Huang and H. J. Fan, *Adv. Energy Mater.*, 2017, **7**, 1700220.
- 19 X. Zou, Y. Liu, G.-D. Li, Y. Wu, D.-P. Liu, W. Li, H.-W. Li, D. Wang, Y. Zhang and X. Zou, *Adv. Mater.*, 2017, **29**, 1700404–1700410.
- 20 J.-X. Feng, H. Xu, S.-H. Ye, G. Ouyang, Y.-X. Tong and G.-R. Li, *Angew. Chem., Int. Ed.*, 2017, **56**, 8120–8124.
- 21 J. Yang, F. Zhang, X. Wang, D. He, G. Wu, Q. Yang, X. Hong, Y. Wu and Y. Li, *Angew. Chem., Int. Ed.*, 2016, **128**, 13046–13050.
- 22 J. Jiang, M. Gao, W. Sheng and Y. Yan, *Angew. Chem., Int. Ed.*, 2016, **128**, 15466–15471.
- 23 W. Zhu, C. Tang, D. Liu, J. Wang, A. M. Asiri and X. Sun, *J. Mater. Chem. A*, 2016, **4**, 7169–7173.
- 24 J. Tian, Q. Liu, A. M. Asiri and X. Sun, *J. Am. Chem. Soc.*, 2014, **136**, 7587–7590.
- 25 P. Xiao, W. Chen and X. Wang, *Adv. Energy Mater.*, 2015, **5**, 1500985.
- 26 Y. Shi and B. Zhang, *Chem. Soc. Rev.*, 2016, **45**, 1529–1541.
- 27 Z. Pu, Q. Liu, A. M. Asiri and X. Sun, *ACS Appl. Mater. Interfaces*, 2014, **6**, 21874–21879.
- 28 L.-N. Zhang, S.-H. Li, H.-Q. Tan, S. U. Khan, Y.-Y. Ma, H.-Y. Zang, Y.-H. Wang and Y.-G. Li, *ACS Appl. Mater. Interfaces*, 2017, **9**, 16270–16279.
- 29 J. M. McEnaney, J. Chance Crompton, J. F. Callejas, E. J. Popczun, C. G. Read, N. S. Lewis and R. E. Schaak, *Chem. Commun.*, 2014, **50**, 11026–11028.
- 30 D. Y. Chung, S. W. Jun, G. Yoon, H. Kim, J. M. Yoo, K.-S. Lee, T. Kim, H. Shin, A. K. Sinha, S. G. Kwon, K. Kang, T. Hyeon and Y.-E. Sung, *J. Am. Chem. Soc.*, 2017, **139**, 6669–6674.
- 31 Y.-Y. Ma, C.-X. Wu, X.-J. Feng, H.-Q. Tan, L.-K. Yan, Y. Liu, Z.-H. Kang, E.-B. Wang and Y.-G. Li, *Energy Environ. Sci.*, 2017, **10**, 788–798.

- 32 H. Furukawa, K. E. Cordova, M. O'Keeffe and O. M. Yaghi, *Science*, 2013, **341**, 1230444–1230455.
- 33 B. Liu, H. Shioyama, T. Akita and Q. Xu, *J. Am. Chem. Soc.*, 2008, **130**, 5390–5391.
- 34 H.-L. Jiang, B. Liu, Y.-Q. Lan, K. Kuratani, T. Akita, H. Shioyama, F. Zong and Q. Xu, *J. Am. Chem. Soc.*, 2011, **133**, 11854–11857.
- 35 C. L. Hill, *Chem. Rev.*, 1998, **98**, 1–2.
- 36 A. Müller, F. Peters, M. T. Pope and D. Gatteschi, *Chem. Rev.*, 1998, **98**, 239–272.
- 37 D.-L. Long, R. Tsunashima and L. Cronin, *Angew. Chem., Int. Ed.*, 2010, **49**, 1736–1758.
- 38 D.-Y. Du, J.-S. Qin, S.-L. Li, Z.-M. Su and Y.-Q. Lan, *Chem. Soc. Rev.*, 2014, **43**, 4615–4632.
- 39 H. B. Wu, B. Y. Xia, L. Yu, X.-Y. Yu and X. W. D. Lou, *Nat. Commun.*, 2015, **6**, 6512.
- 40 Y.-J. Tang, M.-R. Gao, C.-H. Liu, S.-L. Li, H.-L. Jiang, Y.-Q. Lan, M. Han and S.-H. Yu, *Angew. Chem., Int. Ed.*, 2015, **54**, 12928–12932.
- 41 Y. Chen, S. Li, X. Pei, J. Zhou, X. Feng, S. Zhang, Y. Cheng, H. Li, R. Han and B. Wang, *Angew. Chem., Int. Ed.*, 2016, **55**, 3419–3423.
- 42 C.-Y. Sun, S.-X. Liu, D.-D. Liang, K.-Z. Shao, Y.-H. Ren and Z.-M. Su, *J. Am. Chem. Soc.*, 2009, **131**, 1883–1888.
- 43 S. S.-Y. Chui, S. M.-F. Lo, J. P. H. Charmant, A. G. Orpen and I. D. Williams, *Science*, 1999, **283**, 1148–1150.
- 44 P. Pachfule, D. Shinde, M. Majumder and Q. Xu, *Nat. Chem.*, 2016, **8**, 718.
- 45 S. Wei, K. Qi, Z. Jin, J. Cao, W. Zheng, H. Chen and X. Cui, *ACS Omega*, 2016, **1**, 1367–1373.
- 46 M. A. R. Anjum and J. S. Lee, *ACS Catal.*, 2017, **7**, 3030–3038.
- 47 Y. Zheng, Y. Jiao, Y. Zhu, L. H. Li, Y. Han, Y. Chen, A. Du, M. Jaroniec and S. Z. Qiao, *Nat. Commun.*, 2014, **5**, 3783.
- 48 J. Deng, P. Ren, D. Deng, L. Yu, F. Yang and X. Bao, *Energy Environ. Sci.*, 2014, **7**, 1919–1923.
- 49 C. Sun, Q. Dong, J. Yang, Z. Dai, J. Lin, P. Chen, W. Huang and X. Dong, *Nano Res.*, 2016, **9**, 2234–2243.
- 50 J. Tian, Q. Liu, N. Cheng, A. M. Asiri and X. Sun, *Angew. Chem., Int. Ed.*, 2014, **53**, 9577–9581.